

Automated implant segmentation in cone-beam CT using edge detection and particle counting

Ruben Pauwels · Reinhilde Jacobs · Hilde Bosmans ·
Pisha Pittayapat · Pasupen Kosalagood ·
Onanong Silkosessak · Soontra Panmekiate

Received: 4 July 2013 / Accepted: 9 September 2013 / Published online: 29 September 2013
© CARS 2013

Abstract

Purpose To develop a fully automated, accurate and robust segmentation technique for dental implants on cone-beam CT (CBCT) images.

Methods A head-size cylindrical polymethyl methacrylate phantom was used, containing titanium rods of 5.15 mm diameter. The phantom was scanned on 17 CBCT devices, using a total of 39 exposure protocols. Images were manually thresholded to verify the applicability of adaptive thresholding and to determine a minimum threshold value (T_{\min}). A three-step automatic segmentation technique was developed. Firstly, images were pre-thresholded using T_{\min} . Next, edge enhancement was performed by filtering the image with a Sobel operator. The filtered image was thresholded using an iteratively determined fixed threshold (T_{edge}) and converted to binary. Finally, a particle counting method was used to delineate the rods. The segmented area of the titanium rods was compared to the actual area, which was corrected for phantom tilting.

Results Manual thresholding resulted in large variation in threshold values between CBCTs. After applying the edge-enhancing filter, a stable T_{edge} value of 7.5% was found. Particle counting successfully detected the rods for all but one device. Deviations between the segmented and real area ranged between -2.7 and $+14.4 \text{ mm}^2$ with an average absolute error of 2.8 mm^2 . Considering the diameter of the segmented area, submillimeter accuracy was seen for all but two data sets.

Conclusion A segmentation technique was defined which can be applied to CBCT data for an accurate and fully automatic delineation of titanium rods. The technique was validated in vitro and will be further tested and refined on patient data.

Keywords Cone-beam computed tomography · Computer-assisted image analysis · Dental implants · Radiographic phantom · Dentistry

R. Pauwels (✉) · P. Pittayapat · P. Kosalagood · O. Silkosessak ·
S. Panmekiate
Department of Radiology, Faculty of Dentistry, Chulalongkorn
University, Bangkok, Thailand
e-mail: pauwelsruben@hotmail.com

R. Pauwels · R. Jacobs · P. Pittayapat
Oral Imaging Center, OMFS-IMPACT Research Group,
Department of Imaging and Pathology, Faculty of Medicine,
Catholic University of Leuven, Leuven, Belgium

R. Jacobs
Dentistry, University Hospitals Leuven, Leuven, Belgium

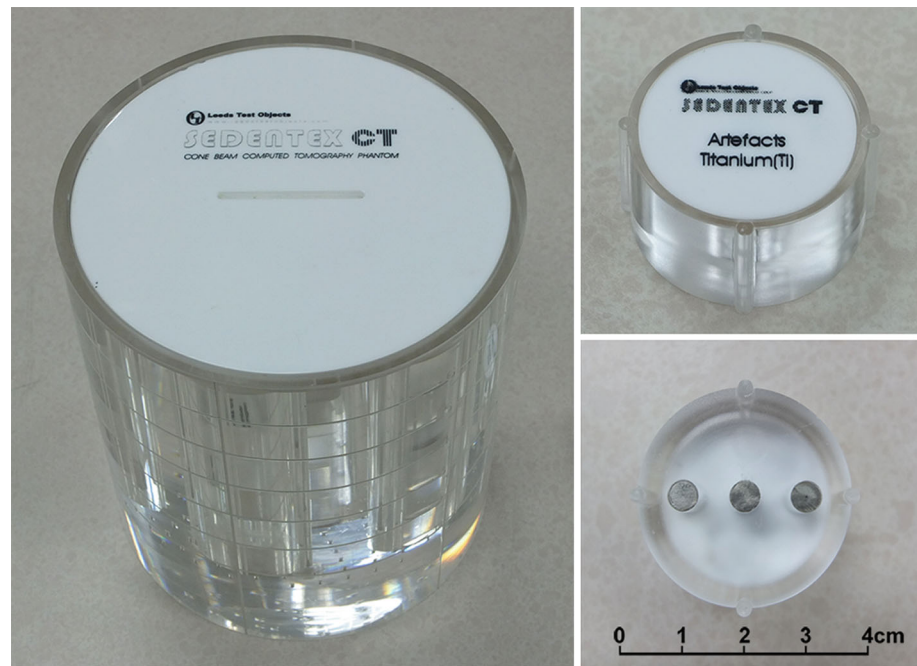
H. Bosmans
Radiology, Department of Imaging and Pathology, Faculty of Medicine,
Catholic University of Leuven, Leuven, Belgium

Introduction

Cone-beam computed tomography (CBCT) is a commonly applied technique for a variety of dental applications, such as implant planning, orthodontics and endodontics. CBCT devices are able to produce three-dimensional images of the oral and maxillofacial region at a high resolution and a relatively low radiation exposure level [1]. CBCT has proven to be particularly useful for the planning and follow-up of dental implant placement.

Regarding the post-operative evaluation of implant location and integration, there have been various reports on the use of CBCT or multi-slice CT (MSCT) for verification of implant position and evaluation of osseointegration and bone

Fig. 1 PMMA phantom (*left*) and insert containing titanium rods (*right*)



architecture in the vicinity of the implant [2–4]. Standardization and clinical acceptance of peri-implant bone analysis on CBCT images will be greatly enhanced if it is possible to accurately delineate the implant on the image. This would enable the evaluation of bone architecture using a region of interest (ROI) at a preset distance from the implant's surface, taking into account that voxels in the immediate vicinity of the implant will be affected by metal artefacts.

In CT imaging, segmentation of objects or tissues is commonly done using thresholding based on prior knowledge of the density of the region of interest. However, it has been shown that grey values cannot be used directly in a quantitative way in CBCT imaging for various reasons, namely excessive X-ray scatter detection, histogram shifting and the effect of tissues outside the scanned volume [5,6]. Therefore, it can be expected that segmentation of metal objects cannot be performed accurately and reproducibly by directly applying a fixed or adaptive threshold, as the ideal threshold value will differ between scanners as well as between images from the same scanner. Furthermore, the image quality of CBCT images is severely hampered due to the presence of metal objects (e.g., dental implants, crowns and fillings, orthodontic brackets) causing metal artefacts [7,8]. These artefacts are typically displayed as dark and bright streaks in the vicinity of the metal objects, further complicating the segmentation of implants on CBCT images.

The objective of this study was to develop a fully automated, robust and accurate method for implant segmentation on CBCT images and to validate it in vitro using titanium rods of known size.

Materials and methods

Test object

A head-size cylindrical polymethyl methacrylate (PMMA) phantom (160 mm diameter, 177 mm height) manufactured by Leeds Test Objects (Boroughbridge, UK) was used (Fig. 1). The phantom contains seven cylindrical holes, allowing the placement of inserts for image quality analysis [9]. A specific type of insert (34.5 mm diameter, 20 mm height) was used in this study. It consists of three titanium rods of 5.15 ± 0.1 mm, fully embedded into PMMA and positioned in a straight line with a distance of 10 mm between the centres (Fig. 2). The size of the rods corresponds to commonly used wide-diameter dental implants [10]. The insert was placed in one of the peripheral columns of the head-size phantom. Empty columns were filled using PMMA inserts.

The phantom was scanned using 17 CBCT devices: 3D Accuitomo 170 (J. Morita, Kyoto, Japan), 3D Accuitomo XYZ image intensifier version (J. Morita), CBMercuray (Hitachi Medical, Tokyo, Japan), CRANEX 3D (Soredex, Tuusula, Finland), DentiiScan (NECTEC & MTEC, National Science and Technology Development Agency, Pathum Thani, Thailand), GALILEOS Comfort (Sirona Dental Systems, Germany), i-CAT Next Generation (Imaging Sciences International, Hatfield, PA, USA), Kodak 9000 3D (Carestream Health, New York, NY, USA), Kodak 9500 (Carestream Health), NewTom VGi (Quantitative Radiology, Verona, Italy), Pax-Uni3D (Value Added Technologies,

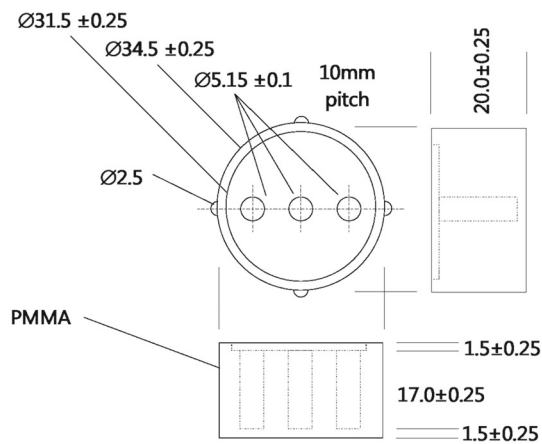


Fig. 2 Schematic drawing of insert containing three titanium rods. All distances are expressed in mm. From SEDENTEXCT IQ phantom user manual, Leeds Test Objects, Boroughbridge, UK

Yongin, Republic of Korea), Picasso Trio (Value Added Technologies), ProMax 3D (Planmeca Oy, Helsinki, Finland), SCANORA 3D (Soredex), SCANORA 3Dx (Evaluation Unit, Soredex), SkyView (Cefla Dental Group, Imola,

Italy), Veraviewepocs 3D (J. Morita) and WhiteFox (Acteon Group, Mérignac, France). The phantom was also scanned with a multi-slice computed tomography (MSCT) device (Somatom Sensation 64, Siemens, Erlangen, Germany). Different exposure protocols were used where possible by varying imaging parameters which are known to affect segmentation accuracy (i.e. FOV size, tube output (mAs), voxel size, peak voltage). All exposure protocols are shown in Table 1.

Reference values for metal area

To verify the efficacy of the segmentation, the actual area of the segmented objects was determined based on their known diameter and the phantom’s tilt (i.e. angle to the z-axis) during each scan. The metal rods in the test object all have a diameter of 5.15 mm with an uncertainty of ± 0.1 mm as estimated by the manufacturer. If the phantom would be positioned exactly level, the axial cross section through the rods would be a circle with an area of $20.8 \text{ mm}^2 \pm 0.8 \text{ mm}^2$. However, it was assumed that there was a slight phantom tilt in some cases, which needed to be corrected for. The axial cross section through the rods was therefore considered as

Table 1 CBCT and MSCT exposure parameters

	FOV (cm)	kVp	mA	Exposure time (s)	mAs	Voxel size (mm)
<i>CBCT</i>						
3D Accuitomo 170	6 × 6; 17 × 12	90	5	31	155	0.08; 0.25
3D Accuitomo XYZ	4 × 3	80	4	18	72	0.125
CBMercuryRay	14.8 × 14.8	80; 120	15	10	150	0.29
Cranex 3D	8 × 6	90	5	12.6	63	0.2
Dentiiscan	16 × 3.4; 16 × 13	90	6	18	108	0.2; 0.4
Galileos Comfort	15 × 15	85	7	4	28	0.29
I-CAT Next Generation	16 × 13; 23 × 16	120	5	3.7; 4.0; 7.3	18.5; 20; 36.5	0.25; 0.3; 0.4
Kodak 9000 3D	5 × 3.6	70	10	11	110	0.076
Kodak 9500	14.5 × 8.3; 20 × 18	90	10	11	110	0.2; 0.3
NewTom VGi	12 × 8	110	4; 12	10; 15	40; 180	0.16; 0.24
PaX-Uni3D	5 × 5	85	6	20 ^a	N/A	0.2
Picasso Trio	12 × 7	85	4.8	15; 24 ^a	N/A	0.2; 0.3
ProMax 3D	8 × 8	84	7; 14	3; 12	21; 168	0.16; 0.32
SCANORA 3D	10 × 7.5	85	8	2.5; 3.8	20; 30	0.2; 0.3
SCANORA 3Dx	10 × 8; 16.5 × 14	90	8	6; 4	48; 32	0.15; 0.2
SkyView	17 × 17	90	6.5	6; 8; 15	39; 52; 98	0.34
Veraviewepocs 3D	8 × 8	70	3	17	51	0.125
WhiteFox	6 × 6; 19.8 × 16.9	105	9	6; 9	54; 81	0.1; 0.3
<i>MSCT</i>						
Somatom Sensation 64	Full	120	127; 139	1	127; 139	0.39

A selection of protocols was made based on the available settings of the device and the clinical relevance of the protocol. Other clinical exposure protocols may be available

FOV field of view

^a These values represent the acquisition (scan) time, as the actual exposure time could not be retrieved from the DICOM header and was not shared by the manufacturer

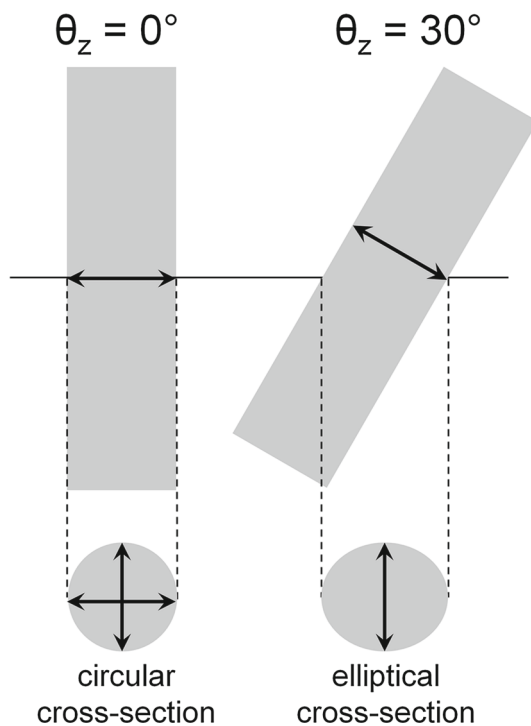


Fig. 3 Effect of phantom tilt on cross-sectional area of the titanium rods. A perfectly vertical rod has a circular axial cross section. A tilt of the rod results in an elliptical cross section. The *small axis* of the ellipse corresponds to the diameter of the rod. The *long axis* is a function of the tilt angle θ_z . A *heavily exaggerated tilt angle* is shown for the purpose of visualization. All lines with double arrows denote equal distances

an ellipse rather than a circle, seeing that the cross section through a cylinder is elliptical for non-zero angles (Fig. 3). The area A of an ellipse is determined as follows:

$$A = \pi ab$$

with a and b as the major and minor radius of the ellipse, respectively. For a cylindrical section, the minor radius corresponds to the radius of the cylinder. To estimate the major radius, the angle of each rod and implant to the z -axis were estimated. As measuring the actual angle would require manual oblique reformatting of the image, which can be prone to error, the angle with the z -axis was measured in the coronal and sagittal planes separately. In a three-dimensional (xyz) Cartesian coordinate system, the angle α_z of a vector to the z -axis can be estimated as follows:

$$\tan^2 \theta_z = \tan^2 \theta_x + \tan^2 \theta_y$$

with θ_x and θ_y the angle between the x - and y -projections (i.e. coronal and sagittal slices) of the vector and the z -axis.

The major radius a of the ellipse is then calculated as follows:

$$a = \frac{r}{\cos(\theta_z)}$$

with r the radius of the cylinder.

Segmentation methods

Method 1: Manual thresholding

Manual thresholding was performed for two purposes. First of all, it was hypothesized that these thresholds would vary considerable between CBCT models and exposure protocols. This would indicate that the determination of a fixed, relative threshold applicable to all CBCT data sets (i.e. a threshold value varying with the minimum and maximum grey value of the image, but at a fixed relative position along the grey scale) would not be feasible. Secondly, manual thresholding served to determine a minimum threshold value for the automatic segmentation method's first step (see following subsection). All images were manually thresholded by a researcher with extensive experience in image analysis using ImageJ (US National Institutes of Health, Bethesda, Maryland, USA). The grey value range was calculated for each data set as the absolute difference between the minimum and maximum grey values within the axial slice, and the position of the threshold within the grey value range was expressed as a percentage with 0 and 100 % corresponding to the minimum and maximum grey values, respectively.

To illustrate the potential variability in manual thresholding due to image display, the phantom scan of the Kodak 9000 3D CBCT was selected. The image was displayed at two extreme grey value display (i.e. 'level') settings and manually thresholded to obtain a segmented area corresponding to the perceived edge of the titanium rods. Resulting areas were compared with the true area of the rods' cross sections as well as the area obtained from the segmentation method proposed below.

Method 2: Pre-thresholding, edge detection and particle counting

All processing and analysis steps were performed within ImageJ. Two pre-processing steps were performed: standardization of the grey value range and pre-thresholding. Firstly, all data sets were transformed to 16-bit to standardize the grey scale. This was done on a slice-by-slice level, ensuring that within each axial slice, the lowest grey value was 0 and the highest 65,535 ($2^{16} - 1$). Although this grey scale transformation was not strictly required for further analysis, it facilitated the application of an overall threshold value and the creation of a binary mask by avoiding that the threshold value needed to be calculated slice-by-slice. Secondly, pre-thresholding was performed to eliminate unwanted edges from the image such as air-PMMA interfaces and artefact-artefact or artefact-PMMA transitions. The lowest of the manually determined threshold values for all CBCT data sets (T_{\min}) was selected as pre-threshold.

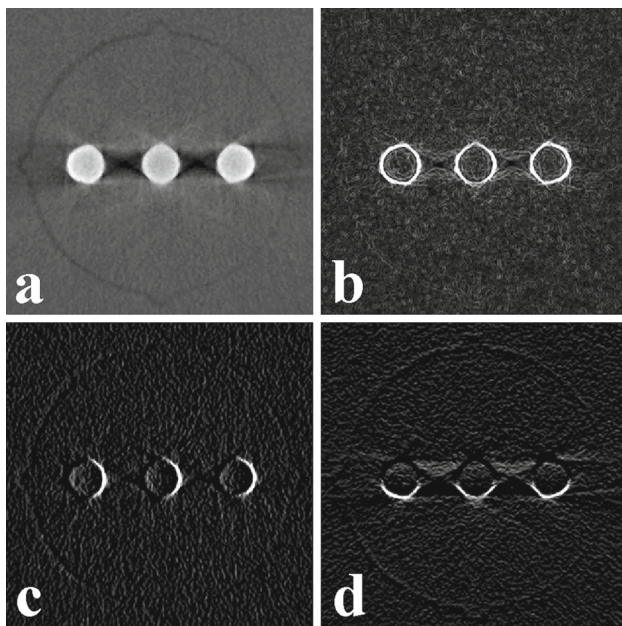


Fig. 4 Sobel operator for edge enhancement. **a** Original image of phantom insert with three titanium rods (Veraviewepocs 3D). **b** Filtered with Sobel operator. **c** x -Component of Sobel operator. **d** y -Component of Sobel operator

Next, all CBCT data sets were filtered with a Sobel operator to highlight edges. The operator uses two 3×3 convolution kernels (S_x and S_y) which calculate the derivative of the image in the x - and y -direction:

$$S_x = \begin{bmatrix} +1 & 0 & -1 \\ +2 & 0 & -2 \\ +1 & 0 & -1 \end{bmatrix} \quad S_y = \begin{bmatrix} +1 & +2 & +1 \\ 0 & 0 & 0 \\ -1 & -2 & -1 \end{bmatrix}$$

The two derivatives are then combined into one output image by calculating the square root of the sum of squares. The output image corresponds to the gradient of the edges in the original image. Figure 4 shows the x - and y -derivatives and the output image.

The edge image was then thresholded with a second threshold value (T_{edge}) and converted into a binary (i.e. black and white) mask. As the Sobel operator rearranged grey values according to the magnitude of the edge in each voxel, it was expected that a consistent T_{edge} could be found for all CBCT data. The optimal T_{edge} value was iteratively determined by attempting various thresholds at continuously smaller intervals and verifying the results.

After thresholding with T_{edge} , the binary image was subjected to particle counting. Particle counting is an application of pixel counting, which is commonly used in the detection and measuring of cells or cellular structures on binary or thresholded microscopy images. The main purpose of using it in this context was to discard loose or grouped voxels outside the area of the titanium rods that were thresholded due to large

local edges. Using this method, the binary image was scanned slice per slice. When a thresholded pixel was encountered, it was grouped together with all connected thresholded pixels within the same axial slice as a particle. The particle was counted and measured if it passed pre-determined size and circularity restrictions. Size limits were expressed in mm^2 , circularity was defined as follows:

$$\text{Circularity} = \frac{4\pi \times \text{Area}}{\text{Perimeter}^2}$$

and ranged between 0 and 1, with 1 corresponding to a perfect circle. Varying values for size range and circularity were investigated, allowing some room for error for both parameters. The size range was initially determined by considering a maximum allowable deviation of one voxel at each side of the titanium rod for a low-resolution image (i.e. voxel size 0.4 mm), resulting in a minimum area of 14.9 mm^2 and a maximum of 27.8 mm^2 . As it was seen that areas were over-estimated for some data sets, the maximum area was adjusted to 37 mm^2 . The minimum circularity was set at 0.5.

All objects that passed particle counting were subsequently fitted to an ellipse to smooth out small aberrations. As initial results showed the segmented areas to be consistently too large, the ellipses were filled and eroded. Using erosion, the outer voxels of the segmented region are removed, as all voxels not fully surrounded by other segmented voxels are turned into background (i.e. white, in this case). After eroding the segmented ellipses, their area was compared to the real area of the rods, taking into account the correction for phantom tilting.

Figures 5 and 6 illustrate the different steps used in the currently proposed segmentation method.

Results

Method 1: Manual thresholding

A histogram showing the manually determined threshold values is shown in Fig. 7. Out of 37 included CBCT data sets, 11 data sets from 5 different devices showed a threshold value close to the maximum grey value. For other data sets, the threshold was found within a wide range, averaging at 72% with a standard deviation of 7%. The position of the threshold value along the grey scale showed no overall consistency between data sets. Different exposure protocols from the same CBCT device generally showed similar threshold values.

Figure 8 illustrates the effect of grey value display on the perceived area of the titanium rods. A difference of 5 mm^2 was seen between segmented areas obtained from the same image displayed using a low and high 'level' setting.

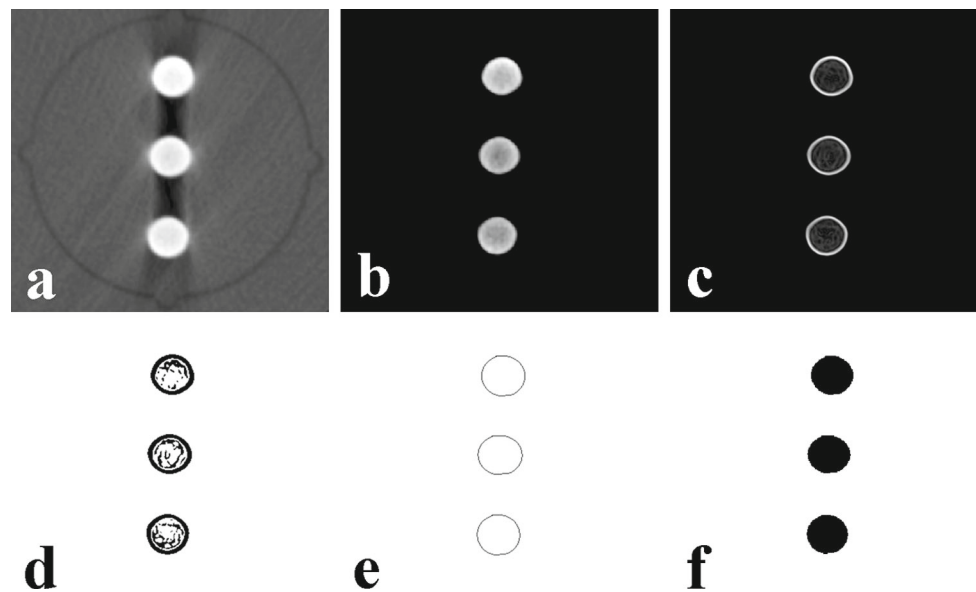


Fig. 5 Successive steps in segmentation method. **a** Original CBCT image (WhiteFox). **b** Pre-thresholded using a T_{\min} of 60%. **c** Filtered using Sobel operator. **d** Thresholded using a T_{edge} of 7.5%. **e** Fitted to an ellipse after particle counting. **f** Filled and eroded

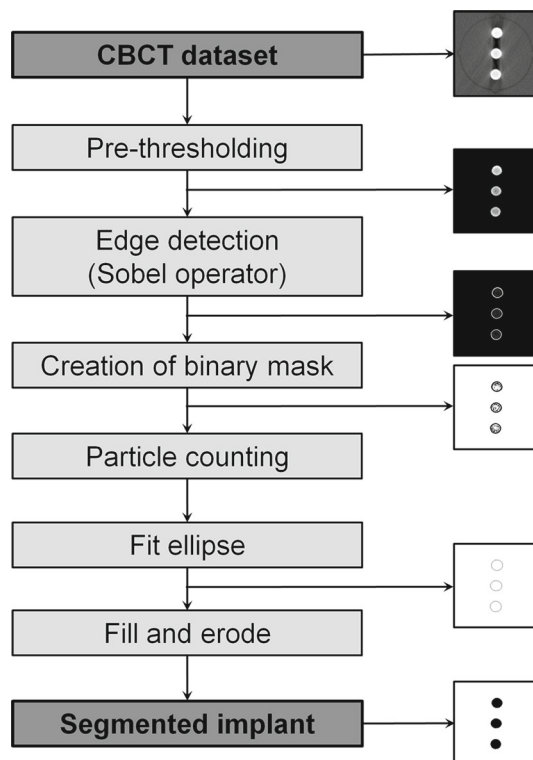


Fig. 6 Flowchart of the different steps involved in the proposed implant segmentation technique. Thumbnails of the images from Fig. 5 are added at their respective position along the segmentation flow

Method 2: Pre-thresholding, edge detection and particle counting

Based on the manually determined thresholds from Fig. 7, a T_{\min} value of 60% was selected as pre-threshold. Figure 9

shows the effect of the pre-thresholding on the edge image. It can be seen that most of the artefacts, noise and unwanted edges were removed after pre-thresholding.

The most optimal T_{edge} value was determined at 7.5%. Many data sets showed reasonable flexibility regarding the choice of T_{edge} , whereas others displayed a more narrow range of applicable thresholds. As the segmentation is fully automated, reproducibility between repeated measurements was perfect. Segmented areas were consistent between the 10 axial slices that were analysed for each data set, with a deviation from the mean area averaging at 0.4%.

For 36 out of 39 data sets, all metal rods were successfully detected. For the three data sets from the SkyView CBCT device, some rods were not segmented. A more adequate segmentation could be obtained for data sets from this model by adapting the segmentation parameters (i.e. increasing the area range and threshold value), but areas were still grossly overestimated. In addition, the increased threshold value was not applicable for several other CBCT data sets. Therefore, it was chosen to optimize the segmentation parameters for all other devices instead.

After correcting for phantom tilting, cross-sectional areas of the titanium rods were between 20.831 and 20.865 mm². For the 36 data sets, which were used to optimize the segmentation algorithm, the smallest error range was obtained by applying a single erosion step before particle analysis, resulting in errors between -2.7 and +14.4 mm² with a median of -0.0 mm². The average of the absolute error values was 2.8 mm². One device (Picasso Trio) showed a relatively large overestimation of the metal area for both of its exposure protocols (+11.5 and +14.4 mm²). The MSCT device (Somatom SENSATION 64) also showed overestimation for both expo-

Fig. 7 Variability of manual thresholding on CBCT images. Histogram showing the location of the manually determined threshold along the grey scale of the image for 39 data sets, with 100% corresponding to the maximum grey value

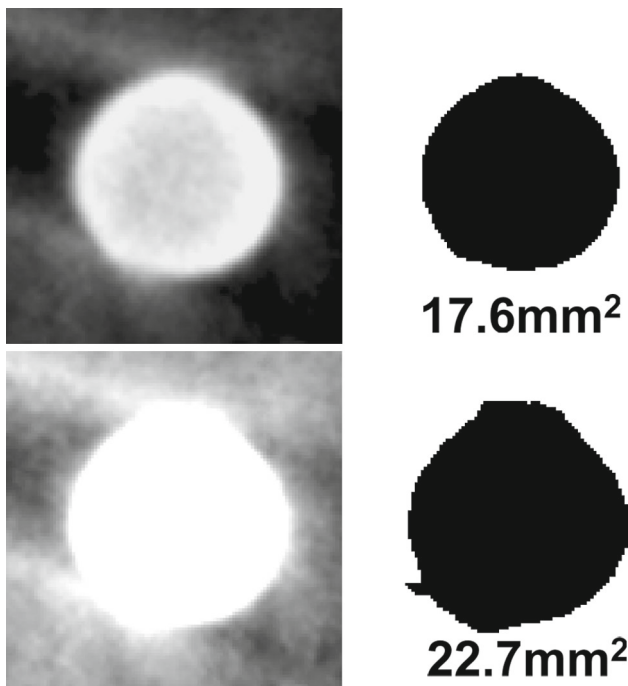
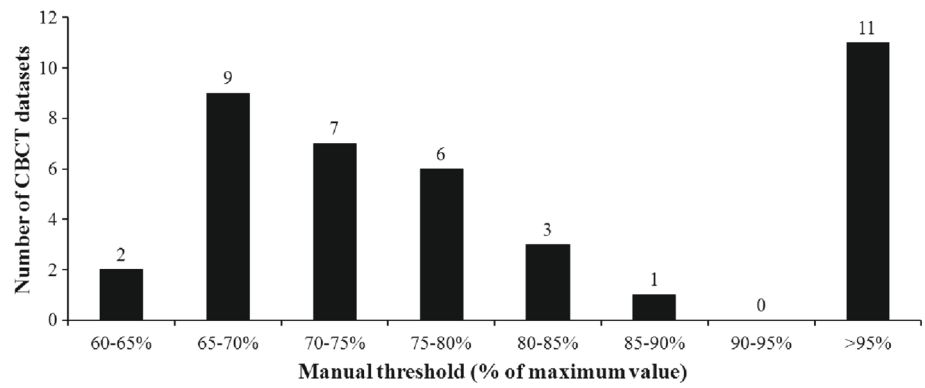


Fig. 8 Potential implant segmentation error from manual thresholding or delineation. Phantom images from Kodak 9000 3D, cropped to highlight one of the titanium rods. *Left column* shows the same rod at different display (i.e. ‘level’) settings. *Right column* shows manually thresholded images of the perceived rod. Areas corresponding to the manual thresholds are provided. Real area of the rod’s cross section: 20.8 mm^2 , area obtained from automatic segmentation using the particle counting method: 21.1 mm^2

sure protocols (+10.2 and +3.0 mm^2). Out of 36 data sets, 28 showed an absolute error of 3.0 mm^2 or lower, with the average absolute error within this group being 1.1 mm^2 .

For eleven data sets, which showed a relatively large degree of oversegmentation, the number of erosions was increased to verify the potential use of a custom number of erosions. For these data sets, the number of erosions required to obtain the most accurate representation of the real area of the titanium rods was either two ($n = 8$) or three ($n = 3$). The gain in accuracy, expressed as the difference in the deviation (%) from the true area, resulting from optimizing the number

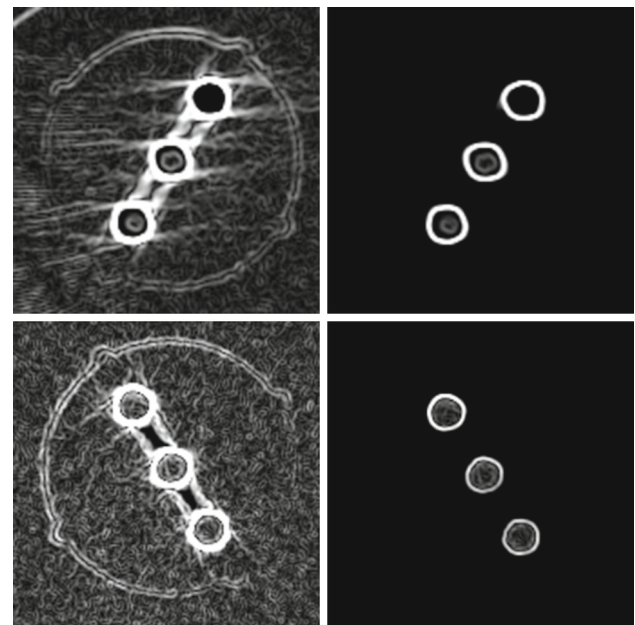


Fig. 9 Effect of pre-thresholding on edge image. *Left column* original edge image. *Right column* edge images after pre-thresholding (60%). *Top row* GALILEOS Comfort, *bottom row* i-CAT Next Generation

of erosions ranged between 1 and 62% with an average of 25%.

The overall average absolute error was reduced from 2.8 to 1.2 mm^2 by using the most optimal number of erosions for each data set. In addition, all errors were below 3 mm^2 . Figure 10 shows the reduction in overall error when using a custom number of erosions compared with the use of a single erosion.

The accuracy of the segmentation was re-calculated in function of diameter of the rods and the voxel size of the data set. When comparing the diameter of the segmented area with the actual diameter of the rod, errors ranged between -0.4 and $+1.6\text{ mm}$. The average absolute deviation from the real diameter was 0.3 mm . Considering the 34 CBCT data sets, the deviation was less than 1 mm for all but two and less than 0.5 mm for all but seven data sets. The linear error

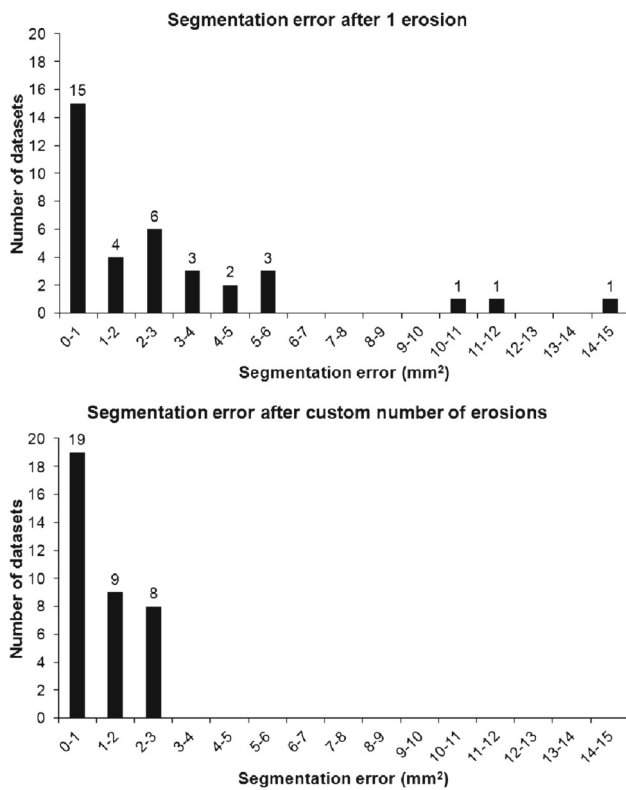


Fig. 10 Histograms comparing the distribution of absolute errors of the segmented area for 36 data sets when using a single erosion (*top*) or a custom number of erosions (*bottom*) after particle counting. Between both histograms, results from 25 out of 36 data sets are unchanged, as multiple erosions only resulted in improved area estimations for 11 data sets

regarding the segmented versus real diameter of the rod was calculated and expressed in voxels. The average deviation was 1.5 voxels, ranging between 0.0 and 6.3 voxels. Similar to the errors in the segmented area, this average was affected by a few data sets with relatively high oversegmentation, as the deviation was 2.0 voxels or lower for 28 out of 36 data sets.

Figure 11 demonstrates the feasibility of the proposed segmentation method on a clinical image using the i-CAT Next Generation CBCT. The image of the selected patient contained two adjacent implants in the upper jaw. Both implants were detected and delineated with no interference from surrounding tissues.

The total runtime of the algorithm using a medium-end workstation was 10–20 s, depending on the size of the data set.

Discussion

In this study, the segmentation of titanium implants on CBCT images was explored. A fully automated segmentation algorithm was developed using a combination of pre-

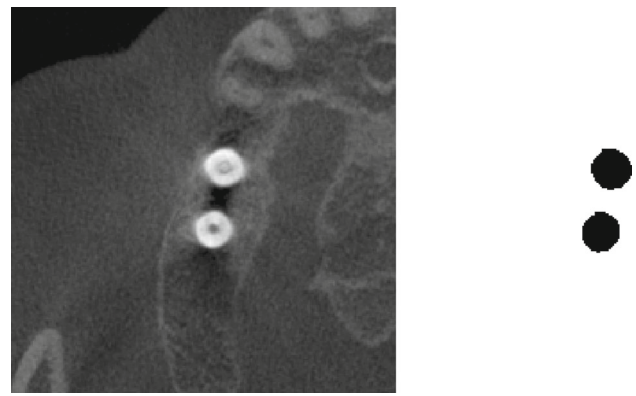


Fig. 11 Applicability of the proposed segmentation method on clinical data. *Left* CBCT (i-CAT Next Generation) image of patient with two adjacent implants in the upper jaw. Image was cropped for the purpose of visualization. *Right* result of implant segmentation using particle counting

thresholding, edge detection and particle counting. The algorithm was optimized and validated in vitro using a head-size PMMA phantom including cylindrical titanium rods of known dimensions.

The algorithm showed considerable accuracy for the majority of the evaluated data sets. When focusing on the diameter of the segmented area versus the real diameter of the titanium rods, the segmentation showed submillimeter accuracy for 34 out of 36 data sets. This can be considered as clinically acceptable, seeing as the immediate vicinity of a dental implant is not clinically useful on a CBCT image due to the presence of different types of metal artefacts [7,8].

Various studies have reported on the segmentation of structures on CBCT images, mostly focusing on anatomical structures such as bones, teeth and air cavities [11–13]. Although it has been proven that CBCT data sets allow for accurately segmentations of regions of varying size, shape and density, the low contrast-to-noise ratio and lack of standardized grey values complicate the application of basic thresholding for automated segmentation.

Although segmentation is mostly performed on anatomical structures, different studies have focused on the segmentation of metallic objects in the oral region on MSCT or CBCT images in the context of metal artefact reduction (MAR) [14–16]. The available literature on MAR shows that a robust, automated technique for the delineation of metal objects on CBCT images has not yet been determined. In particular, previous segmentation methods with demonstrated efficacy on MSCT images may not be directly applicable on CBCT due to its relatively high image noise and the unavailability of standardized grey values. Yazdi et al. use a threshold at 90% of the maximum grey value to segment metallic dental objects for MAR using data replacement [14]. In a study on MAR in head and neck CT, Lell et al. also determine a threshold based on a fixed ratio of the maximum

grey value [15]. The variation between manually determined thresholds for the 17 CBCT devices included in this study shows that this approach, while valid for MSCT, is not feasible for CBCT (Fig. 7). Tohnaek et al. presented a segmentation method for dental CT scans based on a combination of thresholding and filtering of the binary mask using a disc-shaped element [16]. Although this approach can lead to accurate segmentations, the values for the two input parameters (threshold and radius) are expected to vary between CBCT devices.

The segmentation method presented in this study was successfully applied to data sets from all but one of the included CBCT devices. This can be attributed to the particularly poor image quality of this CBCT model, which exhibited a low spatial resolution, high noise and excessive artefacts as confirmed by several studies [7, 17, 18]. It should be noted that a proper segmentation could still be obtained for this device by increasing the T_{edge} value.

Although the edge filter redistributed grey values and facilitated the choice of an appropriate threshold (i.e. T_{edge}) value, it was expected that certain data sets would be over- or under-segmented given the wide variation of grey value distributions in the original images. Although the original objective was to develop a fixed segmentation method valid for all CBCT data sets, it was seen that certain CBCT images show excessive metal blurring or metal artefacts. To cope with these extraordinary cases, a straightforward solution was proposed involving applying multiple erosions (Fig. 10). The amount of erosions needed would have to be determined for each type of CBCT specifically and possibly needs to be verified for each exposure protocol. A one-time ‘calibration’ using a test object such as the phantom used in this study would suffice. Given the large amount of CBCT data already obtained in this study, a list specifying the number of erosions for each type of CBCT data can be used in concordance with the segmentation algorithm. This list can be updated as data from other CBCT models becomes available. The list can serve as a look-up table, and the algorithm can automatically check the required number of erosions (e.g. by matching device-specific information from the DICOM header with this predetermined table).

There are a few limitations to the in vitro set-up used in this study. A cylindrical PMMA phantom was used, similar in size to standard head phantoms for dosimetry and image quality used in MSCT imaging. Although it provides an appropriate representation of the size and average density of an adult human head, it lacks a few defining characteristics. The material surrounding the titanium rods was homogeneous PMMA, whereas the tissues surrounding the dental implants consist of trabecular and cortical bone. A second limitation of the phantom set-up used in this study is the use of perfectly cylindrical titanium rods with a smooth surface. Although loose restrictions on circularity could be

used in this study, it remains to be seen how screw threads and variations in implant shape would affect the accuracy of the segmentation. It should be noted that, even if the original CBCT data are sharp enough to display these slight irregularities of the implant’s surface, there is no clinical purpose for segmenting them as the immediate vicinity of an implant on a CBCT image is affected by metal artefacts. Even if the clinician wishes to evaluate the tissue adjacent to the screw threads, there would be no sense in performing any kind of image processing for segmentation as the original data will suffice for this kind of assessment. Another possible issue for patient images is the occurrence of other metals or high-density objects and tissues in the oral cavity. Fillings, crowns, enamel and other objects could be wrongfully segmented if they pass the predetermined conditions regarding area and circularity. Furthermore, they may induce additional artefacts which may affect the segmentation of the implants. The first issue can be solved by imposing stricter area and circularity ranges than those proposed in this study. Furthermore, when integrating the slice-by-slice segmentations, volumetric restrictions regarding the minimum length or volume of the segmented objects can be implemented. Regarding the effect of artefacts, seeing that fillings and crowns are found at different axial heights compared to implants, it is expected that the effect of artefacts from objects other than implants will be minimal as metal artefacts primarily manifest within the axial plane.

The next step in the validation of the currently developed segmentation technique is to implement it on patient images from various CBCT devices to verify its potential for clinical application. An example is shown in Fig. 11, showing that two implants could be successfully segmented from a patient’s CBCT image. However, true clinical validation of the method would require a large patient sample from different CBCT models. The exact size of each implant would have to be known as well to verify the accuracy of the segmentation. One particular challenge of clinical validation will be to determine an appropriate size range for the particle counting step, ensuring that small- and large-diameter implants pass this criterion.

The prospective application of the developed technique in clinical practice is two fold. As proposed in the introduction, it can be used for automated analysis of CBCT images containing implants, both as a verification of implant position and as a first step in peri-implant bone analysis. An accurate delineation of the implant’s edge would enable the clinician to check and measure the placement of the implant in relation to the surrounding bone and other structures such as the mandibular canal. However, it is not feasible to distinguish the exact edge of the implant, which can lead to considerable errors during manual segmentation (Fig. 8). Automated segmentation could also be used to compare the actual position with the planned position on the pre-operative

image, although in that case, a registration of pre- and post-operative scans may suffice [3]. An important and emerging application of this segmentation technique would be as a first step in the analysis of bone architecture after implant placement using techniques such as morphometric and fractal analysis [19,20]. All of these techniques are highly sensitive to the size and placement of the ROI. Although the most optimal parameters for bone structure analysis are still to be determined, an accurate segmentation of the implant would greatly facilitate the standardization of these techniques.

The second potential application of metal segmentation is found in image reconstruction. MAR algorithms use a variety of approaches to reduce or remove metal artefacts from CT images. Although the literature on MAR is mainly found in the field of medical CT, a few studies on MAR in CBCT are available and different manufacturers have implemented a MAR option [21]. A crucial aspect of any MAR algorithm is to make a distinction between metal and non-metal in order to properly correct the raw data. Severe over- or under-segmentation could lead to improper correction of metal artefacts or the loss of anatomical information in the image. When used in MAR, the currently proposed technique will have to be adapted in order to include all possible metals including fillings, crowns and orthodontic brackets. This can be done by applying looser restrictions on area and circularity during particle counting.

In conclusion, a segmentation technique was defined which can be applied to CBCT data for an accurate and fully automatic delineation of titanium rods. The segmentation method is versatile and allows for further customization towards specific CBCT devices or other metal objects. The technique was validated in vitro and will be further tested and refined on actual dental implants using patient data, focusing specifically on the limitations of the currently used phantom set-up. In addition, the incorporation of this segmentation algorithm as a first step in post-operative bone analysis and MAR will be investigated.

Acknowledgments This study was supported by the Exchange Collaborative Research Grant of the Faculty of Dentistry, Chulalongkorn University, and the Research Fellowship Grant of the European Academy of Dentomaxillofacial Radiology (EADMFR).

Conflict of interest Ruben Pauwels, Reinhilde Jacobs, Hilde Bosmans, Pisha Pittayapat, Pasupen Kosalagood, Onanong Silkosessak and Soontra Panmekiate declare that they have no conflict of interest.

References

1. Scarfe WC, Li Z, Aboelmaaty W, Scott SA, Farman AG (2012) Maxillofacial cone beam computed tomography: essence, elements and steps to interpretation. *Aust Dent J* 57:46–60
2. Naitoh M, Nabeshima H, Hayashi H, Nakayama T, Kurita K, Ariji E (2010) Postoperative assessment of incisor dental implants using cone-beam computed tomography. *J Oral Implantol* 36:377–384
3. Van Assche N, van Steenberghe D, Quirynen M, Jacobs R (2010) Accuracy assessment of computer-assisted flapless implant placement in partial edentulism. *J Clin Periodontol* 37:398–403
4. Wouters V, Mollemans W, Schutyser F (2011) Calibrated segmentation of CBCT and CT images for digitization of dental prostheses. *Int J Comput Assist Radiol Surg* 6:609–616
5. Pauwels R, Nackaerts O, Bellaiche N, Stamatakis H, Tsiklakis K, Walker A, Bosmans H, Bogaerts R, Jacobs R, Horner K, The SEDENTEXCT Project Consortium (2013) Variability of dental cone beam CT grey values for density estimations. *Br J Radiol* 86:20120135
6. Liu Y, Bäuerle T, Pan L, Dimitrakopoulou-Strauss A, Strauss LG, Heiss C, Schnettler R, Semmler W, Cao L (2012) Calibration of cone beam CT using relative attenuation ratio for quantitative assessment of bone density: a small animal study. *Int J Comput Assist Radiol Surg* (Epub ahead of print)
7. Pauwels R, Stamatakis H, Bosmans H, Bogaerts R, Jacobs R, Horner K, Tsiklakis K, The SEDENTEXCT Project Consortium (2013) Quantification of metal artefacts on cone beam computed tomography images. *Clin Oral Implants Res* 24:94–99
8. Schulze R, Heil U, Groß D, Bruellmann D, Dranischnikow E, Schwanecke U, Schoemer E (2011) Artefacts in CBCT: a review. *Dentomaxillofac Radiol* 40:265–273
9. Pauwels R, Stamatakis H, Manousaridis G, Walker A, Michielsen K, Bosmans H, Bogaerts R, Horner K, Tsiklakis K, The SEDENTEXCT Project Consortium (2011) Development and applicability of a quality control phantom for dental cone-beam CT. *J Appl Clin Med Phys* 12:245–260
10. Mijiritsky E, Mazor Z, Lorean A, Levin L (2013) Implant diameter and length influence on survival: interim results during the first 2 years of function of implants by a single manufacturer. *Implant Dent* 22:394–398
11. Loubele M, Maes F, Schutyser F, Marchal G, Jacobs R, Suetens P (2006) Assessment of bone segmentation quality of cone-beam CT versus multislice spiral CT: a pilot study. *Oral Surg Oral Med Oral Pathol Oral Radiol Endod* 102:225–234
12. Liu Y, Olszewski R, Alexandroni ES, Enciso R, Xu T, Mah JK (2010) The validity of in vivo tooth volume determinations from cone-beam computed tomography. *Angle Orthod* 80:160–166
13. Shi H, Scarfe WC, Farman AG (2006) Upper airway segmentation and dimensions estimation from cone-beam CT image datasets. *Int J Comput Assist Radiol Surg* 1:177–186
14. Yazdi M, Lari MA, Bernier G, Beaulieu L (2011) An opposite view data replacement approach for reducing artifacts due to metallic dental objects. *Med Phys* 38:2275–2281
15. Lell MM, Meyer E, Kuefner MA, May MS, Raupach R, Uder M, Kachelriess M (2012) Normalized metal artifact reduction in head and neck computed tomography. *Invest Radiol* 47:415–421
16. Tohnak S, Mehnert AJ, Mahoney M, Crozier S (2011) Dental CT metal artefact reduction based on sequential substitution. *Dentomaxillofac Radiol* 40:184–190
17. Pittayapat P, Galiti D, Huang Y, Dreesen K, Schreurs M, Souza PC, Rubira-Bullen IR, Westphalen FH, Pauwels R, Kalema G, Willems G, Jacobs R (2013) An in vitro comparison of subjective image quality of panoramic views acquired via 2D or 3D imaging. *Clin Oral Investig* 17:293–300
18. Pauwels R, Beinsberger J, Stamatakis H, Tsiklakis K, Walker A, Bosmans H, Bogaerts R, Jacobs R, Horner K, The SEDENTEXCT Project Consortium (2012) Comparison of spatial and contrast resolution for cone-beam computed tomography scanners. *Oral Surg Oral Med Oral Pathol Oral Radiol* 114:127–135

19. Hua Y, Nackaerts O, Duyck J, Maes F, Jacobs R (2009) Bone quality assessment based on cone beam computed tomography imaging. *Clin Oral Implants Res* 20:767–771
20. Hohlweg-Majert B, Metzger MC, Kummer T, Schulze D (2011) Morphometric analysis—cone beam computed tomography to predict bone quality and quantity. *J Craniomaxillofac Surg* 39:330–334
21. Bechara BB, Moore WS, McMahan CA, Noujeim M (2012) Metal artefact reduction with cone beam CT: an in vitro study. *Dentomaxillofac Radiol* 41:248–253